Tidal flushing and eddy shedding in Mount Hope Bay and Narragansett Bay: An application of FVCOM

Liuzhi Zhao,[1] Changsheng Chen,[1] and Geoff Cowles[1]

[1] The tidal motion in Mt. Hope Bay (MHB) and Narragansett Bay (NB) is simulated using the unstructured grid, finite-volume coastal ocean model (FVCOM). With an accurate geometric representation of irregular coastlines and islands and sufficiently high horizontal resolution in narrow channels, FVCOM provides an accurate simulation of the tidal wave in the bays and also resolves the strong tidal flushing processes in the narrow channels of MHB-NB. Eddy shedding is predicted on the lee side of these channels due to current separation during both flood and ebb tides. There is a significant interaction in the tidal flushing process between MHB-NB channel and MHB-Sakonnet River (SR) channel. As a result, the phase of water transport in the MHB-SR channel leads the MHB-NB channel by 90°. The residual flow field in the MHB and NB features multiple eddies formed around headlands, convex and concave coastline regions, islands, channel exits and river mouths. The formation of these eddies is mainly due to the current separation either at the tip of the coastlines or asymmetric tidal flushing in narrow channels or passages. Process-oriented modeling experiments show that horizontal resolution plays a critical role in resolving the asymmetric tidal flushing process through narrow passages. With a horizontal resolution of 50 m, FVCOM reproduces the eddy field that is in good agreement in the intensity and spatial scale with the current measurement data.

1. Introduction

[2] Mt. Hope Bay (MHB) and Narragansett Bay (NB) are located on the northeastern coast of the United States with connection to both Massachusetts and Rhode Island (Figure 1). In some literature, MHB is identified as northeastern NB [*Hicks*, 1959]. Two narrow channels control the water exchange between MHB and NB: the East Passage (MHB-EP) in the southwestern end of MHB and the Sakonnet River (MHB-SR) in the southeastern end. The narrowest widths of the MHB-EP and MHB-SR channels are about 800 and 70 m, respectively. The combined MHB and NB regions comprise an area of about 3.7×10^8 m^2, with an average water depth of about 5.5 m and a maximum depth of about 46 m in the southern part of the EP.

[3] Irregularly shaped islands, inlets, and rivers characterize this integrated bay system. It is a typical shallow water bay that is forced by tides, winds and river discharges. Tidal motion is dominated by the semidiurnal M_2 tide, with the amplitude of the surface elevation ranging from about 0.45 m at the entrance to 0.6 m at the head of the bay

[*Gordon and Spaulding*, 1987]. The phase difference between the entrance and northern reaches is only 6° or 12 minutes, except near the narrow channel where the lag can be significant [*Gordon and Spaulding*, 1987]. In general, the M_2 tide accounts for about 80% of the total current energy [*Kincaid*, 2006]. The ratios of N_2/M_2, S_2/M_2, and K_1/M_2 or O_1/M_2 are about 0.25, 0.2 and <0.15, respectively. The tide-generated sea level amplitudes are less than 0.5 m during neap tide but can exceed 1.0 m during spring tide.

[4] Freshwater discharge into the MHB-NB derives primarily from three major rivers: the Taunton River at the northeastern head of MHB, and the Blackstone and Pawtuxet Rivers at the northwestern head of NB. The Providence River, which sometimes appears in the literature, refers to the combination of Blackstone and Pawtuxet Rivers [*Kincaid*, 2006]. Annual average discharge rate, which is estimated based on the outflow data from 1929–2003, is about 14 m^3/s for the Taunton River, 22 m^3/s for the Blackstone River, and 10 m^3/s for the Pawtuxet River. The peak of individual river discharge usually occurs in December and March and the maximum monthly-averaged discharge rate can exceed 80 m^3/s. Although the total river discharge rate into the MHB and NB is much smaller than the major rivers in the western Gulf of Maine and southeastern US coast, it is the essential process driving the near-surface stratification and buoyancy-driven flow in the bay [*Weisberg*, 1976].

[5] Unlike other eastern US continental shelf regions, the wind field over the MNB-NB features strong temporal and

---

[1]School for Marine Science and Technology, University of Massachusetts at Dartmouth, New Bedford, Massachusetts, USA.
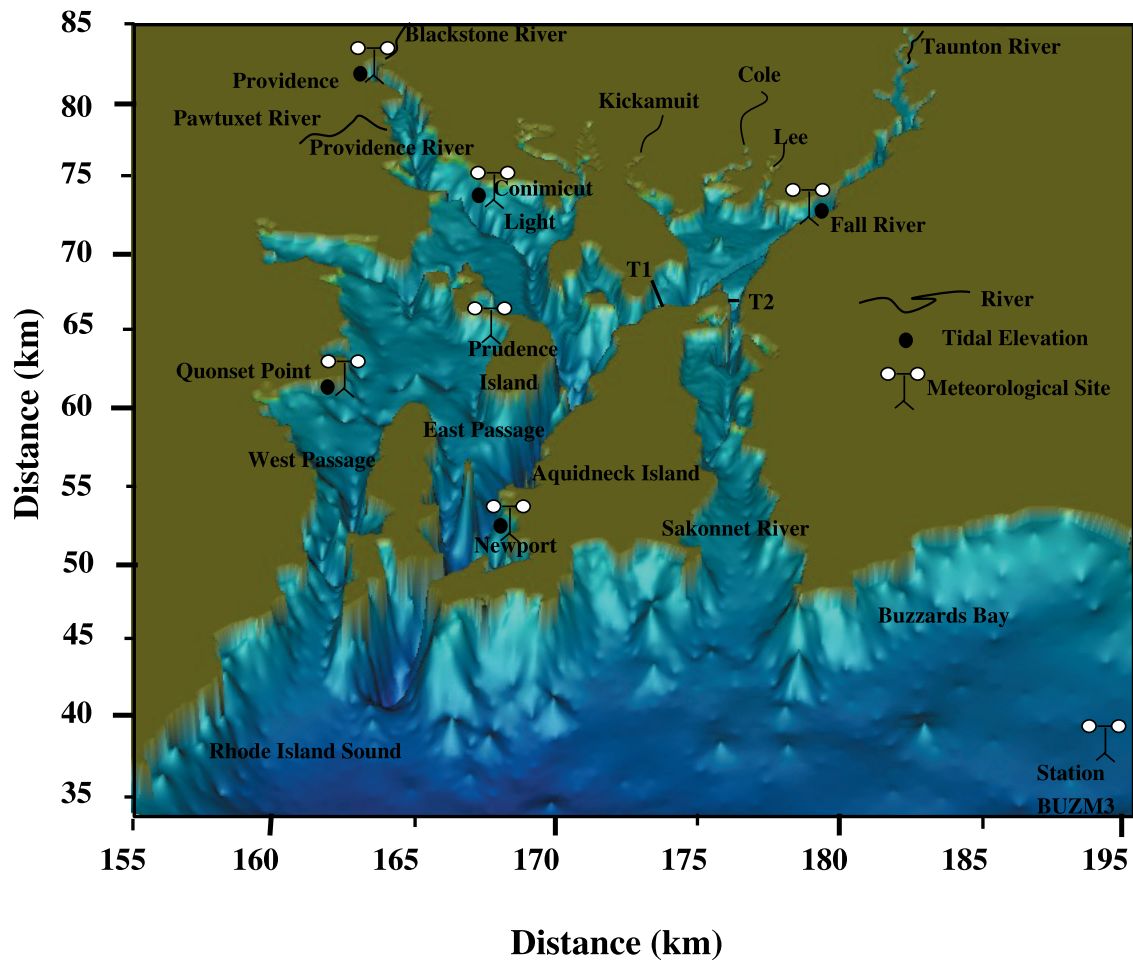
Figure 1. Bathymetry of the Mount Hope Bay (MHB) and Narragansett Bay (NB). T1 and T2 are the URI August 1996 ADCP survey transects and also the transects used to present the vertical profiles of model-predicted tidal currents and water transport.

spatial variability. Coherence analysis of the wind direction at five meteorological stations at Fall River, Conimicut Pt, Providence, Prudence Island, Quonset Pt. and Newport shows a correlation coefficient of 0.8 or higher in the along-coastal direction but not in the cross-coastal direction, suggesting that the seabreeze is an important factor for the local wind variation. This is consistent with our previous analysis of historic wind records, which shows that the wind direction changes dramatically in a short-time scale, so that there is no significant seasonal pattern in the direction throughout the year in the bays. The extent of the wind variation in this area implies that the wind-driven circulation and mixing in the MNB-NB is mainly controlled by the short-term wind variability.

[6] Recently, concerns have been raised that the water stratification in MHB and NB has been significantly increased due to climate warming and hot water released from a nearby power plant. The near-surface water temperature in the entire coastal region of Massachusetts and Rhode Island has increased about 1.1°C since 1965 [*Nixon et al.*, 2004]. The water in the bays, which remained vertically well-mixed throughout the year in 1954–55 [*Hicks*, 1959], was found to be strongly stratified during the late summer of 2001 and 2002 in the entire bay, especially in the Provi-

dence River [*Deacutis et al.*, 2006]. It is believed that the occurrence of the low DO concentration area (or hypoxia) in the Providence River is due to the reduced air-sea exchange and mixing as a result of this increased stratification [*Bergondo et al.*, 2005]. Hot water injected from the power plant in MHB represents an anthropogenic source of heat to the bay water. This water is drawn from the bay, used to cool the working fluid at the plant, and is discharged at a rate of about 40 m³/s. The inflow temperature ranges from 3°C in winter and 24°C in late summer and the discharge ranges from 10°C in winter to 30°C in late summer, representing a consistent increase of about 6.5°C. Since this water is discharged into the MHB as a current jet, it is unclear if this water tends to increase the overall vertical stratification since it also contributes to increased mixing through shear instability.

[7] Previous field measurements clearly show that stratification, mixing, and circulation vary significantly in space and time [*Gray*, 1884; *Haight*, 1938; *Weisberg*, 1976; *Weisberg and Sturges*, 1976]. Since the dynamical system in this area is fully nonlinear and characterized with strong small- and meso-scale variability, it is difficult to understand the local dynamics controlling this shallow system using

only field measurements due to insufficient sampling in space and time.

[8] Some modeling efforts have been made to examine the impact of tides, winds, and river discharge as well as the hot water plume on the stratification and circulation in the MHB-HB [*Gordon and Spaulding*, 1987; *Swanson and Jayko*, 1987; *Spaulding et al.*, 1999]. *Gordon and Spaulding* [1987] applied a traditional structured grid finite-difference model to simulate the tidal motion in NB. Driven by the M_2 and M_4 tidal constituents at the open boundary, their model provided a reasonable result of the M_2 and M_4-induced tidal waves that are in good agreement with tidal measurement at tidal gauges. The differences between model-predicted and observed surface elevations at 11 measurement sites for M_2 tide were $-0.7 - 2.8$ cm in amplitude and $-0.9 - 4.1°G$ in phase, respectively. A more accurate tidal simulation was conducted by *Spaulding et al.* [1999], who included 37 tidal constituents in their numerical experiments and showed a root mean square error of -8.7 cm for the sea surface prediction at available tidal measurement stations.

[9] Narrow inlets often have strong asymmetry in the tidal currents, with potential flow-like behavior upstream and inertial jet-like behavior downstream [*Stommel and Farmer*, 1952]. This is supported by the recent ADCP current measurement across the MNB-EP and MNB-SR channels, which clearly implied the existences of eddies as a result of tidal flushing [*Kincaid*, 2006]. Structured grid models used in previous studies do not resolve the coastal geometry of the channels because experiments were made with insufficient horizontal resolution. Although these models provide a reasonable simulation of the tidal elevation (which is controlled by the water transport), they fail to resolve the realistic field of the tidal currents, particularly in the tidal flushing process. A strong tidal current jet through a narrow channel may generate double eddies on the lee side of tidal flushing. The existence of eddies during tidal flushing can enhance the water exchange rate through the channel [*Wells and Heijst*, 2003]. Failure to capture the tidal flushing process through narrow channels in the MHB-NB would underestimate the water exchange between MHB and the rest of NB.

[10] In this study, we have applied an unstructured grid finite-volume coastal ocean model (called FVCOM) to examine the tidal dynamics in the MHB-NB. This model was developed originally by *Chen et al.* [2003] with the goal of resolving the complex dynamics in estuaries and coastal oceans. Taking advantage of FVCOM's geometric flexibility, we have studied the sensitivity of the model simulation to horizontal resolution. It is the first attempt to introduce a high resolution, mass conservative unstructured grid model in this bay. Numerical experiments using this model clearly demonstrate a need for acute model resolution to resolve realistic tidal flushing process in the MHB-NB.

2. FVCOM and Design of Numerical Experiments

[11] The numerical experiments made in this study were conducted by using FVCOM: a prognostic, unstructured grid, finite-volume, free-surface, three-dimensional (3D) primitive equation coastal ocean and estuarine model de-

veloped by *Chen et al.* [2003]. FVCOM utilizes a modified Mellor and Yamada level 2.5 (MY-2.5) and Smagorinsky turbulent closure schemes for the default setup of vertical and horizontal mixing, respectively [*Mellor and Yamada*, 1982; *Galperin et al.*, 1988; *Smagorinsky*, 1963]. Unlike existing coastal finite-difference and finite-element models, FVCOM solves the hydrostatic primitive equations by calculating fluxes resulting from a discretization of the integral form of these equations on an unstructured triangular mesh. A state-of-the-art σ-transformation is used to represent the vertical coordinate. This approach not only takes advantage of finite-element methods for grid flexibility and finite-difference methods for numerical efficiency but also provides a good numerical representation of momentum, mass, salt, and heat conservation. The detailed description of FVCOM was given in user manual written by *Chen et al.* [2004] and example of model validations and applications can be viewed directly at the website: http://codfish.smast.umassd.edu.

[12] The MHB-NB FVCOM is configured with unstructured triangular meshes covering the entire MHB-NB (Figure 2). The computational domain is bounded in the inner shelf with an open boundary line running from the Rhode Island Sound to Buzzards Bay. To examine the sensitivity of tidal flushing-generated eddy shedding to the horizontal resolution in the MHB-EP channel, numerical experiments were first made using a mesh with the horizontal resolution of about 50 m in the narrow channels, around islands, and along the coast in the MHB (Figure 2a) and subsequently with a mesh with reduced horizontal resolution of about 200 m in the MHB (Figure 2b). In both cases, the horizontal resolution in the remaining area of NB were the same, being around $350 - 450$ m in the upper NB, 800 m in the lower NB, and 3000 m in the inner shelf connected to the open boundary. Total numbers of the nodes and triangles are 6426 and 10747 respectively for the coarse resolution mesh case and 17408 and 32354 for the fine resolution mesh case.

[13] It should be pointed out here that 200 m presents the upper bound of the horizontal resolution used in previous finite-difference models, so that the results obtained from the comparison of the fine and coarse meshes in this study should be applicable to all previous model studies in this region. MHB-NB modeling efforts were supported by the Brayton Point Power Station in Somerset, Massachusetts with the objective of examining the impact of the hot-water injection from the power generator on the marine environment in MHB-NB. The meshes shown in the MHB for the fine mesh case were designed to resolve the hot-water jet and its spatial variation.

[14] The mean water depth at each node point was specified using the bathymetric database obtained from Geophysical Data System (GEODAS) of National Geophysical Data Center (NGDC), NOAA. This database covers the entire the bay region with over 75 hundred thousand measurement samples. Since all the bathymetric samples were referred to the Mean Lower Low Water (MLLW), a depth adjustment was made for the interpolated bathymetric field to set up the mean water depth.

[15] The model is driven by tidal forcing specified at the open boundary. Five major tidal constituents (M_2, N_2, and S_2 for the semidiurnal tide and K_1 and O_1 for the diurnal tide) are considered in the tidal simulation. The amplitudes
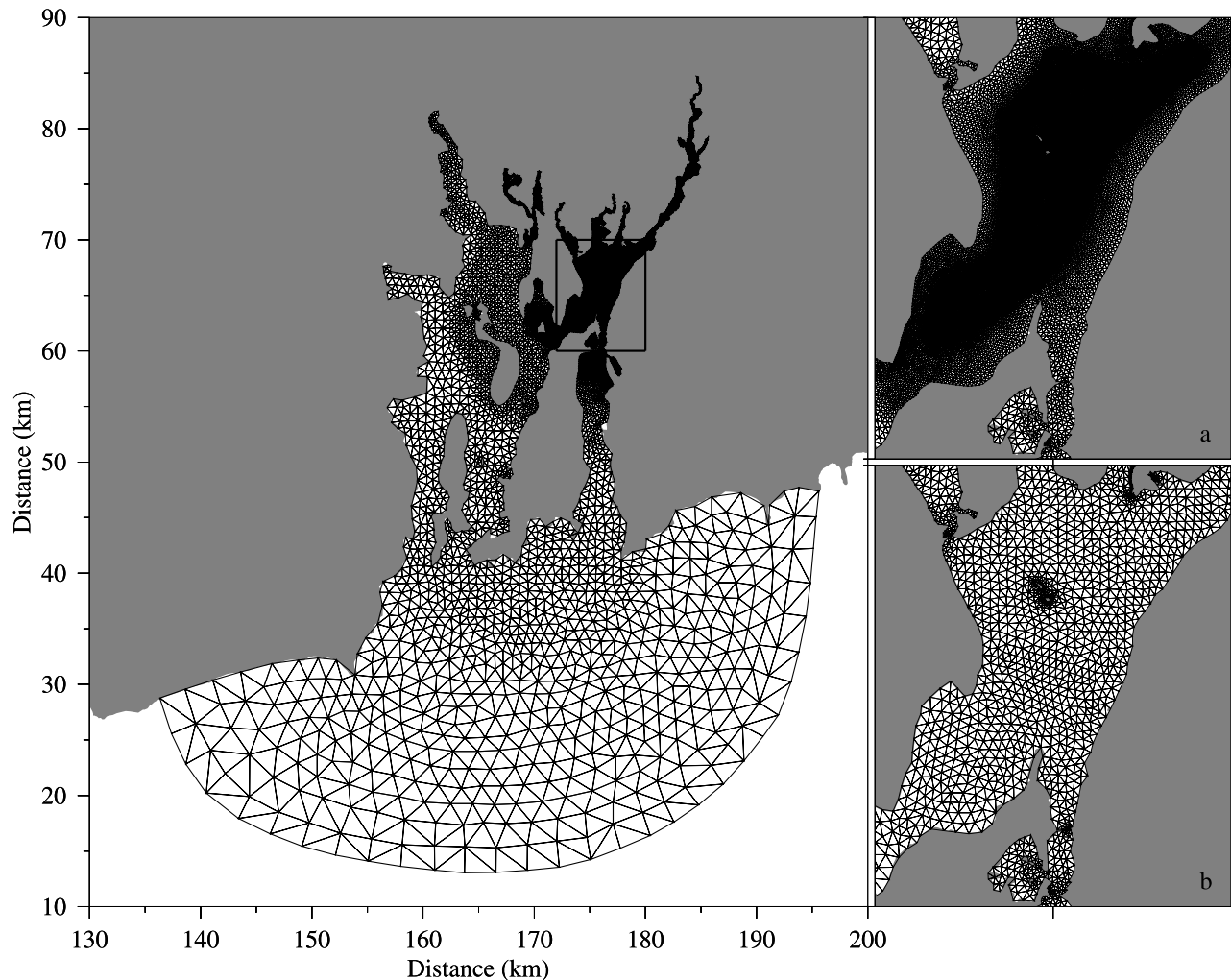
Figure 2. Unstructured triangular meshes of the FVCOM MHB-NB computational domain (left). Two types of meshes are used in numerical experiments: (1) fine meshes (a) with a horizontal resolution of $30-50$ m in the MHB and (2) coarse grid (b) with a horizontal resolution of 200 m in MHB except near islands.

and phases of these tidal constituents at the open boundary are specified using the model output of the Gulf of Maine FVCOM (C. Chen et al., Tidal dynamics in the Gulf of Maine and New England Shelf: An application of FVCOM, submitted to *Deep Sea Research*, 2005), with justification to have the best overall fit to the observed tidal amplitudes and phases at available tidal gauges inside the bays. A tidal database is built by using the model-simulated amplitudes and phases of five major tidal constituents. With implementation of *Foreman* [1977] tidal forecast program, this database is used to set up the initial conditions of the sea level and tidal currents at each grid point and tidal forcing at the open boundary for the real-time tidal simulation and forecast.

3. Model Results

3.1. Tidal Elevation

[16] A tidal-induced inertial-gravity wave propagates into the NB-MHB from the inner shelf with a dominant frequency at the M_2 tidal constituent. The model-predicted M_2 co-tidal chart shows that co-amplitude lines are generally laid across the bay with a slight shift to the southeast-northwest direction (Figure 3). This indicates that at the same latitude, the tidal elevation is slightly higher on the right side of the bay than on the left side of the bay. This is consistent with a coastal inertial gravity wave in which the boundary topography balances the Coriolis force. The tidal amplitude is about $46-48$ cm at the entrance of the bay and increases gradually to $58-59$ cm at the northern end. Co-phase lines lie in the southwest-northeast direction, which suggests that the wave phase propagates slightly faster on the right side of the bay than on the left of the bay. The phase difference from the entrance to the northern end is $8°$, indicating that it only takes about 17 minutes for the M_2 tidal wave to arrive at the northern end from the entrance. At the same latitude, the phase in the MNB lags the phase in the upper NB by about $1-2°$. Such a small tidal phase difference links MHB and NB as a dynamically integrated water system.

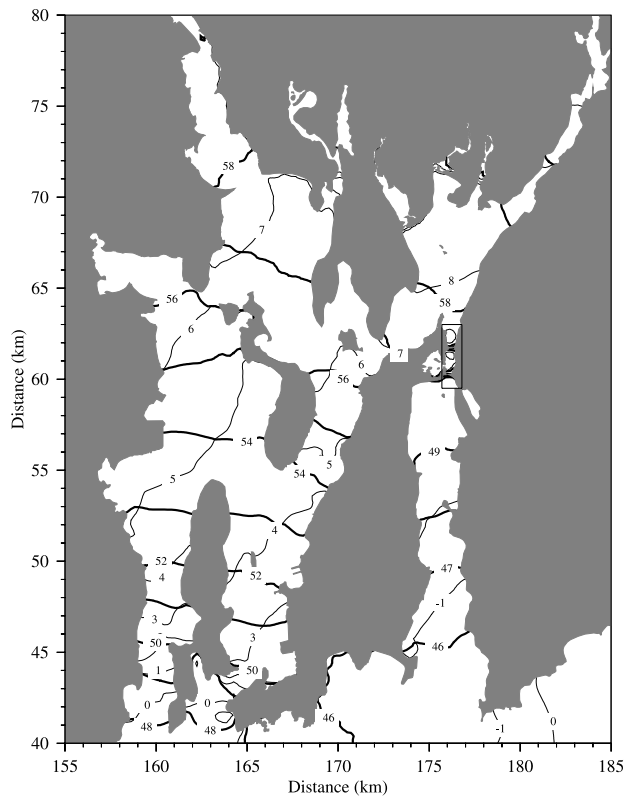[17] FVCOM predicts a remarkable jump in both the amplitude and phase of the M_2 tide on the northern and

Figure 3. Co-tidal chart of the model-predicted M_2 tidal elevation. Heavy solid line: Co-amplitude (cm) and thin solid line: co-phase (°G).

southern side of the Sakonnet River Narrows (SRN) (Figure 4). SRN is very narrow with a length of about 1500 m, a mean water depth of 7 m. There are two narrow necks in SRN, one is at Sakonnet River Bridge (SRB) with a width of about 70 m and another is at Stone Bridge (SB) (linking SRN with MHB and the Sakonnet River) with a width of about 120 m. The amplitude at the southern side of SRN is about 50 cm, while it increases to 57 cm on the northern side of SRN. The difference in sea level is about 3 cm across SB and SRB, separately. Tidal phase is about 1° on the southern side of Narrows and jumped to 4° on the northern side of SB. A similar phase jump is also found on southern and northern sides of SRB. This feature seems real because it is consistent with the field measurement by *Gordon and Spaulding* [1987].

[18] To our knowledge, no previous modeling efforts have resolved this unique feature in the MHB-SR channel [*Gordon and Spaulding*, 1987; *Spaulding et al.*, 1999]. This is not surprising, because all those models were configured with a horizontal mesh size of at least 200 m, about 3 times bigger than the width of the narrow neck. Unlike the finite-difference models, FVCOM uses an unstructured triangular mesh with a horizontal resolution of less than 50 m in the MHB-SR channel. The fact that FVCOM succeed in capturing the sharp jump of the tidal elevation in this channel suggests that the horizontal resolution is a key issue that must be taken into account in the MHB-NB modeling.

[19] The tidal simulation is validated by a direct comparison with observed amplitudes and phases of five major tidal constituents at available tidal gauges around the coast

of the MHB-NB (Figure 5). The standard deviations between model-predicted and observed amplitudes and phases are 0.22 cm and 0.16°G for M_2 tide, 1 cm and 0.66°G for S_2, 0.06 cm and 0.69°G for N_2, 0.11 cm and 0.66°G for K_1, and 0.05 cm and 0.84°G for O_1, all of which are within the range of the measurement uncertainty (Figure 5). Using tidal amplitudes at these five tidal gauges, we calculated the ratio of tidal constituents: they are 0.22 for S_2/M_2; 0.25 for N_2/M_2; 0.12 for K_1/M_2; 0.09 for O_1/M_2, which suggests that M_2 tide accounts for about 70–90% energy of the tidal motion in the bay.

[20] Inputting the model-predicted amplitudes and phases of five tidal constituents into the *Foreman* [1977] tidal forecast program, we set up the initial fields of the tidal elevation and currents (the vertical velocity is calculated using the continuity equation based on the model-predicted tidal elevation and horizontal currents) at all nodes (for the elevation and vertical velocity) and centers (for the horizontal velocity) of triangular meshes and a time series of tidal forcing at the open boundary for the real time hindcast or forecast tidal simulation. An experiment was made for March–April 2001 to check if the model can capture the spring and neap tidal cycles. Comparison with the time
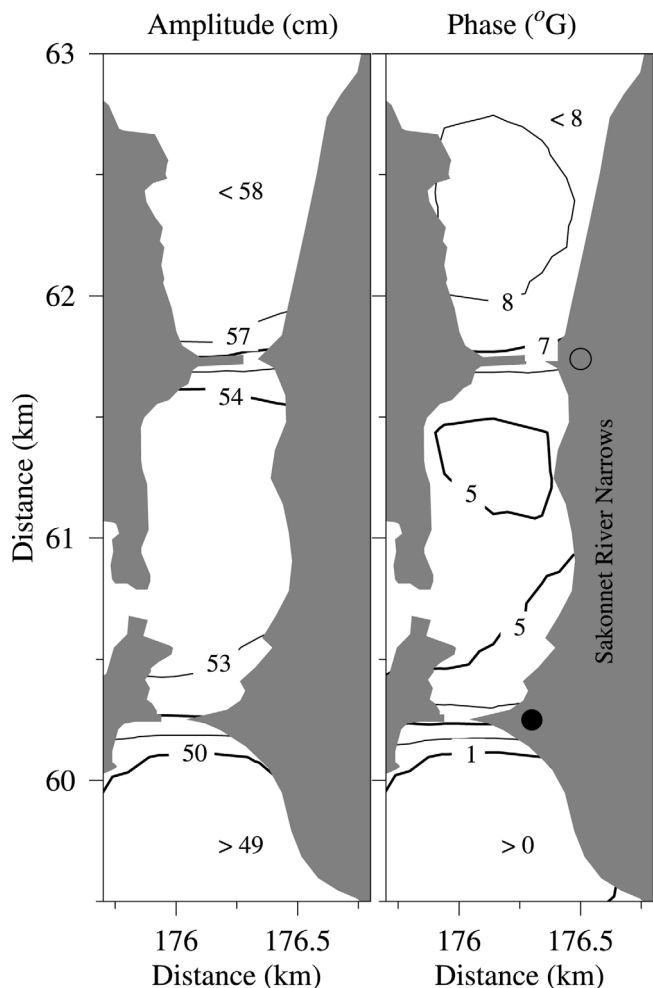

Figure 4. Co-amplitudes (cm) (left) and co-phases (°G) (right) of the M_2 tidal elevation in the MHB-SR channel. Open circle, the Sakonnet River Bridge; solid circle, the Stone Bridge.

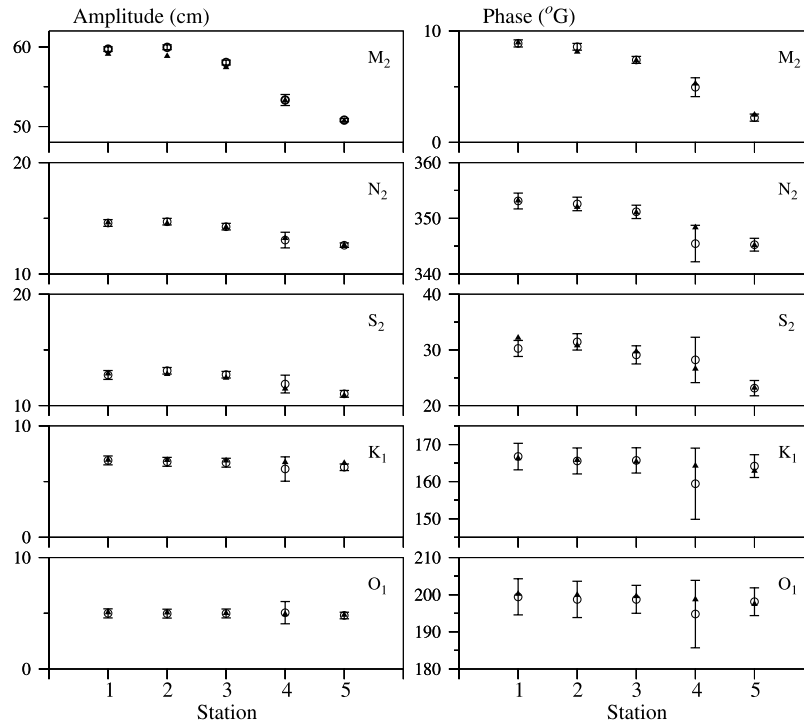**Figure 5.** Comparison between model-predicted and observed amplitudes (cm) and phases (°G) of M_2, N_2, S_2, K_1 and O_1 tidal constituents at five tidal gauges labeled 1 (Fall River), 2 (Providence), 3 (Quonset Point), 4 (Conimicut Light) and 5 (Newport). Open circle, observed; solid triangle, model-predicted. The thin line through open circle is the measurement uncertainty.
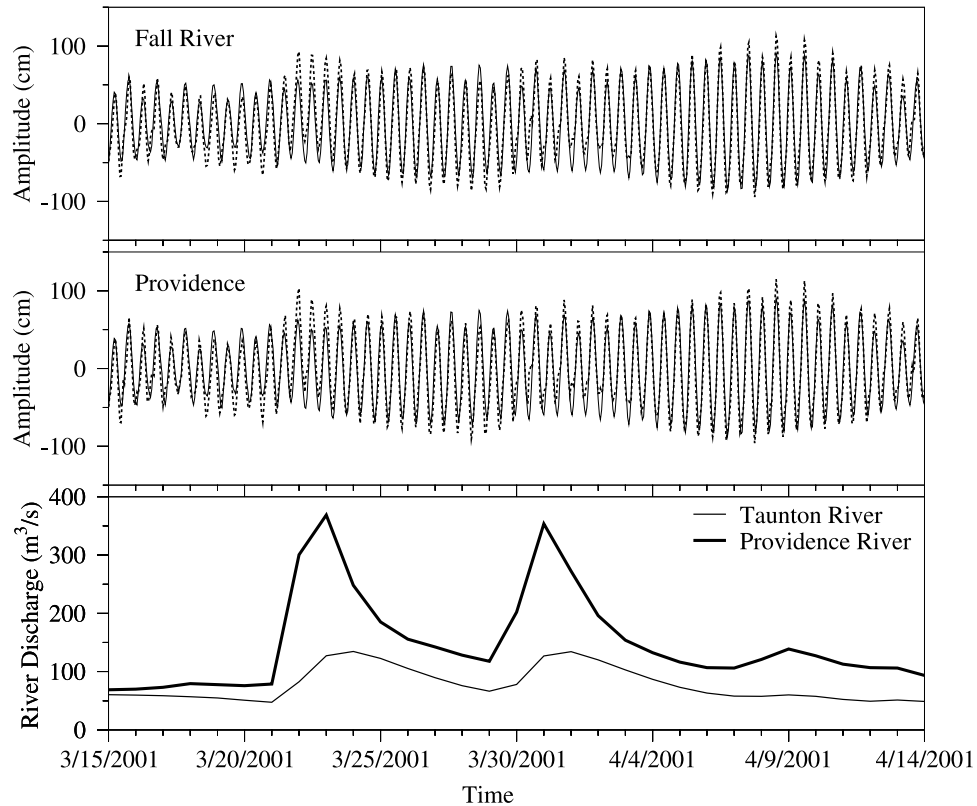

Figure 6. Comparison of model-predicted and observed sea levels at Fall River and Providence sites (top and middle) and river discharge rates at the Providence River and Taunton River (bottom) during March 15 to April 15, 2001. In the top two panels: solid line represents the model-predicted value and dashed line is the observed value.
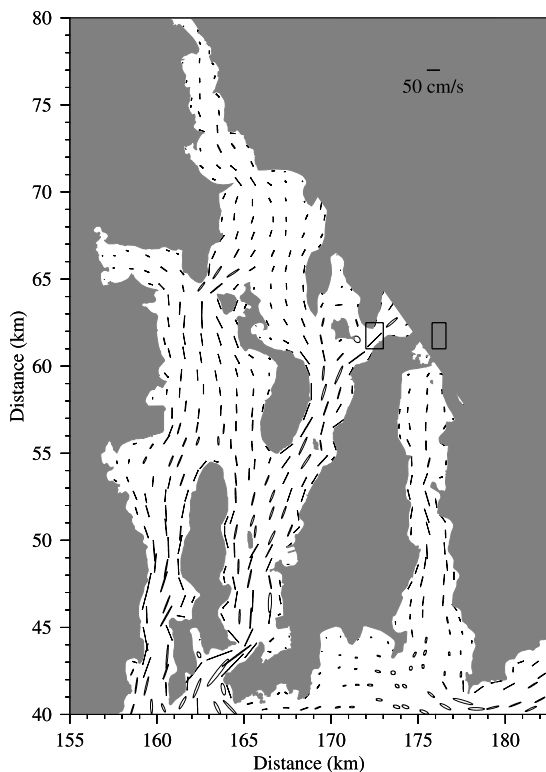
Figure 7. The M_2 tidal current ellipse chart for selected sites from the model results. Two boxes are the selected regions in the MHB-NB and MHB-SR channels used for Figure 8.

series of the observed tidal elevation at five tidal gauges shows that the model is robust enough to capture the spring-neap tidal variation at these sites. Around the time of peak river discharge, the sea level rises, which causes the time series shift above the reference level. Examples can be seen around the two peak periods occurring 20–25 March and 30 March–3 April 2001 at the Fall River and the Providence River (Figure 6), during which the high and low water levels is significantly higher than the tidal-produced values. This suggests that river discharge needs to be taken into account in tidal simulations near the mouth of rivers, especially during the peak season. The comparison also shows some bias in the time series during a spring tide with low river discharge. Since the bias seems to occur at both peak and trough, we assume it is due to an insufficient number of tidal constituents in the tidal simulation.

3.2. Tidal Current Ellipses

[21] Tidal currents in the MHB and NB vary significantly with location, strongest in the narrow channels and passages and weaker near the coast. The M_2 tidal velocity is about 100 cm/s in channels and passages, with the maximum velocity of >120 cm/s occurring at the southern end of the East Passage. Tidal ellipses are oriented along the coastline and local isobath (Figure 7). In the MHB-NB channel, the M_2 tidal current varies along the local isobath, strongest in the deep channel and weaker on both coastal sides (Figure 8a). In the MHB-SR channel, the tidal current is strongest at SRB (over 150 cm/s) and SRN, and is significantly higher on the eastern coast than on the western coast (Figure 8b).

On both the southern and northern corners of the western boundary of the SRB are found the weakest tidal currents, having magnitudes of less than 10 cm/s. These types of tidal shadow areas can be found near the coast of other channels and passages, suggesting that tidal currents are spatially asymmetric across the channel in SRN.

3.3. Tidal Flushing and Eddy Shedding

[22] Tidal currents exhibit asymmetric properties in narrow channels and around islands in MHB and NB. In the MHB-SR channel, for example, the water movement is characterized by strong tidal flushing. During the flood period (defined by rising sea level at the Fall River tidal gauge), the water, originating from the East Passage flow around Hog Island, merges on the eastern side of the Island, and then flushes into the MHB through the deep channel (Figure 9). On the lee side of flushing, two eddies form on lateral sides of the current jet near the maximum flood tide. The one on the eastern side enlarges in size with its center migrating northeastward with time after the maximum flood, while the other on the western side becomes stronger due to the increase of the southward along-coast tidal current during the late phase of the flood period. Similarly, two eddies also occur on the lee side of the tidal flushing during the ebb period: the one on the northern coast forms near the maximum ebb, and the other on the southern coast appears 1–3 hours after the maximum ebb (Figure 10). This is a typical example of eddy shedding due to tidal flushing through a deep narrow channel [*Wells and Heijst*, 2003].

[23] Tidal flushing results in the significant variability of the vertical and horizontal shear of tidal currents during the tidal cycle. For example, in the cross-channel transect (labeled T1 in Figure 1) the along-isobath tidal current is almost uniform in the vertical during the early flood, with a maximum speed in the center of channel and decreasing toward the coast (Figure 11: upper-left). This pattern remains until the maximum flood, when a velocity reversal occurs on the northern coast due to eddy shedding and the axis of the maximum tidal current shifts toward the southern side (Figure 11: middle-left). Two hours after the maximum flood, however, a strong vertical shear occurs in the deep
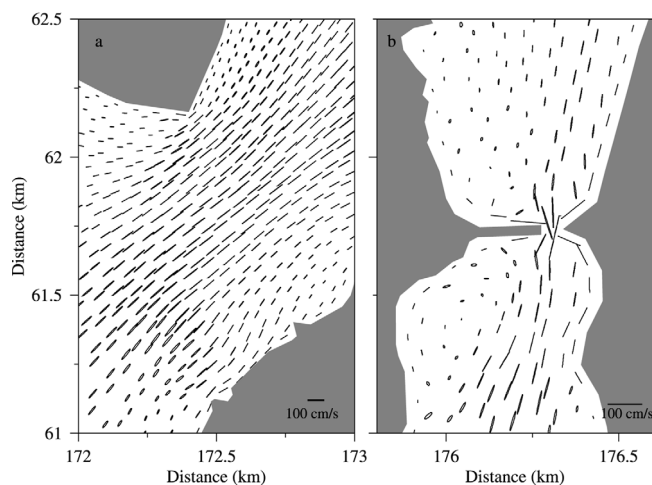

Figure 8. The M_2 tidal current ellipse chart for selected regions in the MHB-NB and MHB-SR channels shown in Figure 7. (a) MHB-NB region; (b) MHB-SR region.
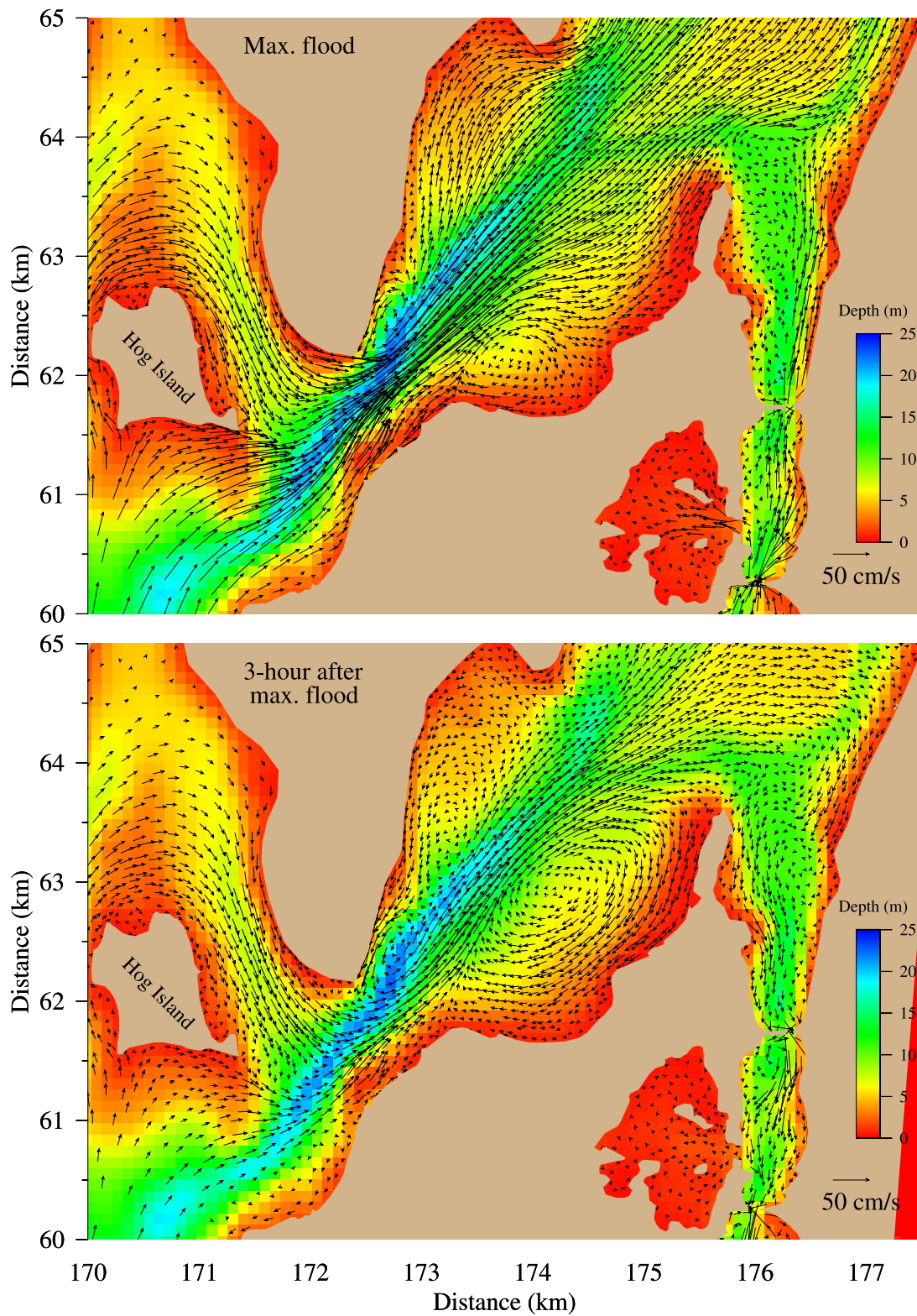
Figure 9. The distributions of the near-surface tidal current at the maximum flood and 3 hours after the maximum flood in the southern part of the MHB-NB-SR regions. The color image shows the bathymetry with depth scales from 0 to 25 m. The number of current points is reduced in the high-resolution region to provide a viewable picture under the limited page size.
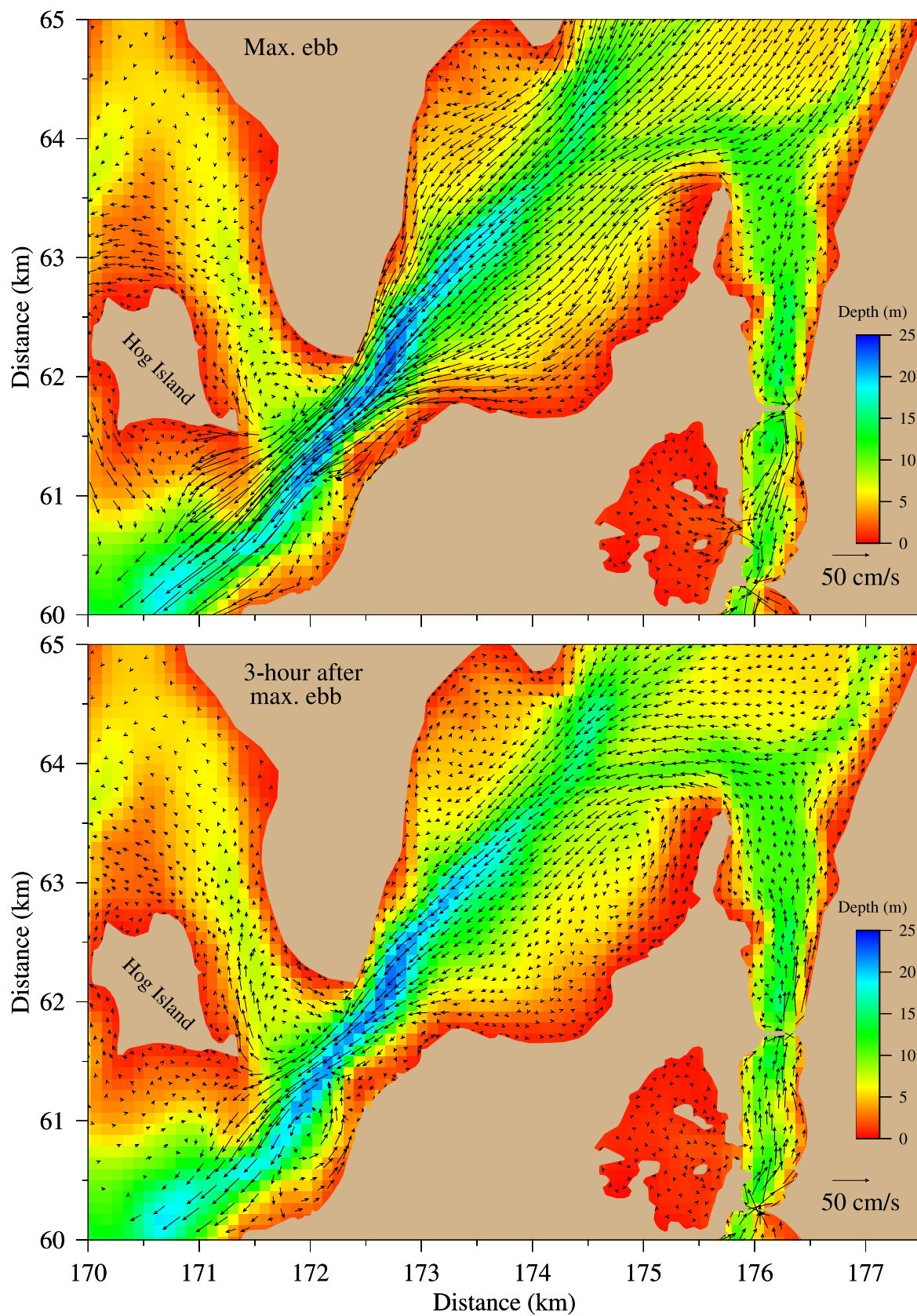
Figure 10. The distributions of the near-surface tidal current at the maximum ebb and 3 hours after the maximum ebb in the southern part of the MHB-NB-SR regions. The color image shows the bathymetry with depth scales from 0 to 25 m. The number of current points is reduced in the high-resolution region to provide a viewable picture under the limited page size.
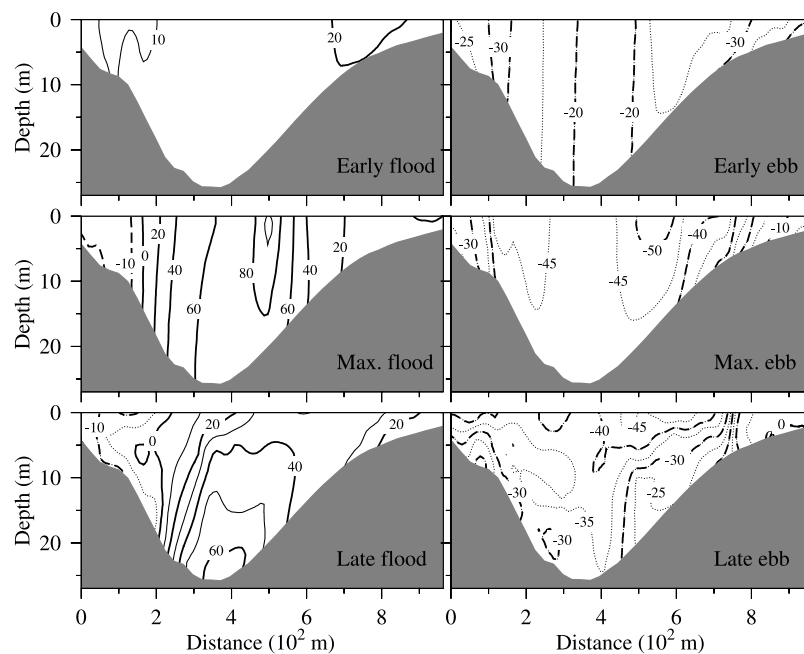
Figure 11. Distribution of the along-isobath tidal current on the transect T1 at early flood (2 hours before the maximum flood), maximum flood, late flood (2 hours after the maximum flood), early ebb (2 hours before the maximum ebb), maximum ebb, and late ebb (2 hours after the maximum ebb). Positive: the inflow to the MHB, and negative: the outflow from the MHB.

channel, with maximum current near the bottom, decreasing toward the surface (Figure 11: lower-left). At this time, the water in the upper 10 m tends to shift toward the southern coast, which is consistent with the formation of a large clockwise eddy in the southern coastal area. The velocity returns to a uniform vertical profile again during the early phase of the ebb period, with a maximum outflow on the slope of the channel about 2 km away from the coast on both sides of the transect (Figure 11: upper-right). A significant vertical shear of tidal currents occurs at the maximum ebb, with the maximum velocity at the surface, decreasing with depth (Figure 11: mid-right). The vertical profile of tidal currents becomes much more complex in the later phase of the ebb period, during which the outflow is stronger on the southern coast than on the northern coast and is strongest at the surface (Figure 11: lower-right).

[24] The tidal flushing in the MHB-NB channel has a direct impact on the current in the MHB-SR channel. For example, at the maximum flood (in the MHB-NB intersection area), there is a strong near-surface tidal current flowing into the MHB from the eastern side of the SR (Figure 9: upper panel). This water merges with the northeast current at the northern exit of the MHB-SR channel and then flows northward along the eastern coast of MHB. Just 3 hours after the maximum flood, an eddy generated on the southwestern coast turns the current clockwise and directs the flow into the MHB-S channel. As a result, the near-surface current in the MHB-SR channel southward reverses southward and flows out of the MHB through the channel (Figure 9: lower panel). Similarly, at the maximum ebb, the near-surface water moves southward in the MHB-SR channel (Figure 10: upper panel), but it reverses 3 hours later due to the presence of a cyclonic eddy in the southwestern coastal region of the MHB (Figure 10: lower panel).

[25] The vertical structure of the tidal currents in the MHB-SR channel significantly differs over a tidal cycle. On transect T2, in the early phase of the flood period, the current is dominated by the inflow through the channel, with a maximum at a mid-depth of about 7.5 m from the surface (Figure 12: upper-left). At the maximum flood, the inflow current shifts toward the eastern coast with the maximum velocity at the surface and reduced vertical shear (Figure 12: mid-left). Consequentially, a weak, vertically uniform outflow occupies the western half of the channel and also the part of the east coast. In the late phase of the flood period, the outflow occupies the entire near-surface layer across the channel and the western half of the channel, while the inflow in the eastern half of the channel significantly reduces, with a maximum velocity at the depth of 5–10 m below the surface (Figure 12: lower-left). Similarly, in the early phase of the ebb period, the tidal current was dominated by a surface-intensified outflow across the entire transect (Figure 12: upper-right). During maximum ebb, the edges of the transect near the coasts contain weak inflow. As a result, the area of the outflow significantly shrinks and its intensity also decreases by about 50% (Figure 12: mid-right). In the late phase of the ebb period, a large portion of the area of the transect is dominated by the inflow with a maximum velocity near the surface on the eastern coast (Figure 12: lower-right).

[26] The interaction of tidal flushing in the MHB-NB and MHB-SR channels causes a 90° phase shift of the water transport in these two regions. An example is shown in Figure 13 for the water transport across transects T1 and T2 around the spring tidal period. The water transport in the MHB-SR channel leads the water transport in the MHB-NB channel by 90°, even though its transport volume is about 3−7 times smaller. The tidally driven water volume trans-
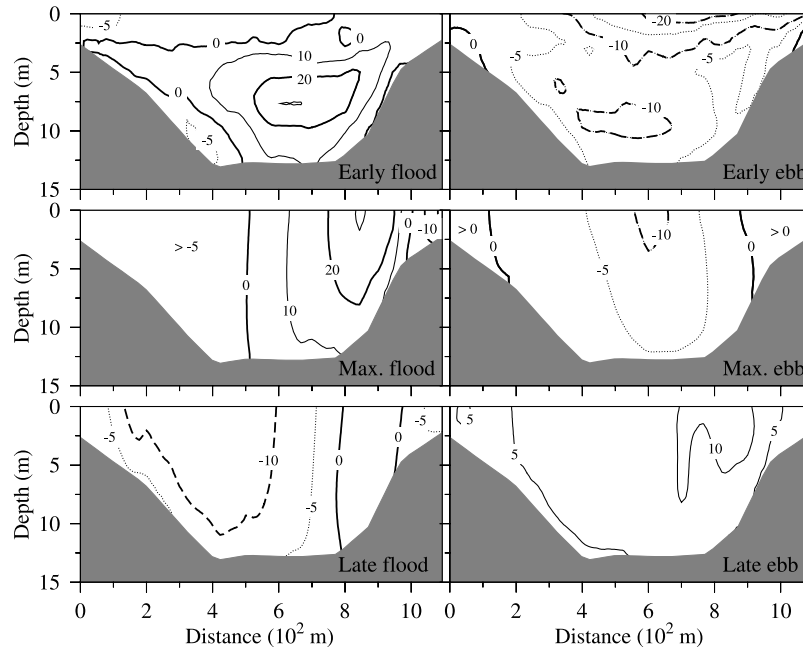
Figure 12. Distribution of the along-isobath tidal current on the transect T2 at early flood (2 hours before the maximum ebb), maximum flood, late flood (3 hours after the maximum ebb), early ebb (2 hours before the maximum ebb), maximum ebb, and late ebb (3 hours after the maximum ebb). Positive: the inflow to the MHB, and negative: the outflow from the MHB.

port through the MHB-NB channel varies with time during the tidal cycle, with a maximum volume of $>5 \times 10^3$ m^3/s (0.005 Sv) at spring tide, while the maximum transport volume through the MHB-SR channel is less than 10^3 m^3/s.

[27] The model-predicted eddy shedding and water transport process are consistent with the August 1996 ADCP field measurements on T1 and T2 (with repeated tracks over tidal cycles) made by Kincaid and co-workers [*Kincaid*, 2006]. His transect current records on T1 show that the tidal current in the deep channel can exceed 100 cm/s at the time of maximum flood, during which the reversed outflow was detected around the northwestern coast region. This finding supports our model results, which indicate that tidal flushing generates a cyclonic eddy in the northwestern coastal region

on transect T1: the reason why a reversed current was measured around the maximum flood. Model-computed magnitude of tidal current is also in good agreement with ADCP records, with a maximum velocity of >100 cm/s at the maximum flood and a significant variability in the vertical shear of the current.

[28] *Kincaid* [2006] used the repeated transect ADCP measurement data to estimate the water transport on transects T1 and T2. He found that the water transport on T2 is 90° out of the phase with the transport on T1. This result is the same as our model computation, indicating that FVCOM resolves the realistic water transport process in the MHB-NB system. Kincaid reported that the water transport estimated from the ADCP measurements was 7.5×10^3
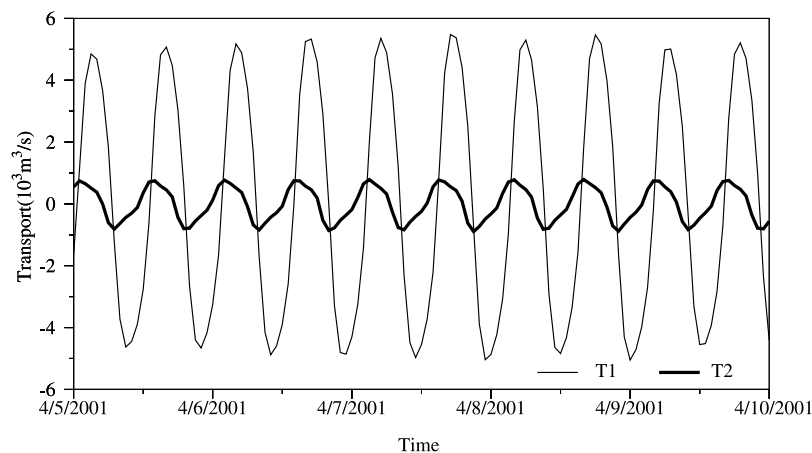

Figure 13. The time series of the tidal-driven water transport through transects T1 (thin solid line) and T2 (heavy solid line) around the spring tide in April 2001.

and 4.5×10^3 m³/s on T1 at the current peak of the spring tide and at the current peak of the tidal cycle a week before spring tide, respectively, while the water transport through T2 was about 10% of the transport through T1 for both cases. Our model results show that in the neap tidal period, the smallest water transport through T1 and T2 are 2.4×10^3 and 0.5×10^3 m³/s respectively. In the spring tide period, the largest water transport through T1 and T2 are 5.5×10^3 and 0.8×10^3 m³/s, respectively. The model-computed ratio of the water transport of T1 to T2 is 14.5% at the spring tide and 21% at the neap tide.

[29] Our model-computed ratio at the spring tide is in good agreement with the estimation made from the ADCP measurement, although they were made under different conditions. The ADCP surveys, taken during the spring tide in August 1996, represent an annual peak of the spring tide in that year, while the model estimation was made using the tidal simulation result at the spring tide in early April 2001. Tidal records show that the tidal range at spring tide in August 1996 is about 50 cm larger than that at spring tide in early April 2001, so it is not surprising that on T1 the transport estimated from that ADCP survey data is larger than the model-computed value. In addition, the ADCP measurements were made in the stratified summer season under realistic wind conditions. The water transport estimated from the ADCP data thus includes the wind-driven component, while the model-computed results are forced only by five major tidal constituents. Considering the differing tidal and wind conditions, FVCOM seems to capture qualitatively the water transport in the MHB-NB and MHB-SR channels.

[30] Flow fields featuring multiple eddies have been widely recognized in local community around this area. The model-predicted eddy shedding areas are in agreement with the distributions of eddies detected by scientists and fishermen, even though no comprehensive current measurements were available to verify the sizes and intensity of these eddies. Kincaid's ADCP measurements were the first to show the existence of a tidal flushing generated eddy in the western coastal area of the MHB-NB channel. Several hydrographic/ADCP surveys were made by Kincaid and his co-workers in 2001 and later. These surveys covered much larger regions of MHB and NB, and many of the model-predicted eddies were detected from these recent data (C. Kincaid, personal communication).

3.4. Residual Flow

[31] Tidal flushing and asymmetry of tidal currents over tidal cycles generates a complex eddy-featured residual flow field in the MHB and NB (Figure 14). The convex coast or headland is generally characterized by a pair of cyclonic and anticyclonic eddies, while two big anticyclonic eddies are predicted in the concave coastal regions in the southwestern region of the MHB. Residual currents in the MHB-NB channel are featured by multiple eddies: a pair of cyclonic and anticyclonic eddies around the northern convex coast plus big anticyclonic eddies on the southwestern coast of the MHB and around the southeastern convex coast of the Hog Island. On the northern side of Hog Island is the clockwise-rotated strong along-coastal residual flow. This water moves southeastward to join the complex eddy field in the northern part of the East Passage southwest of the
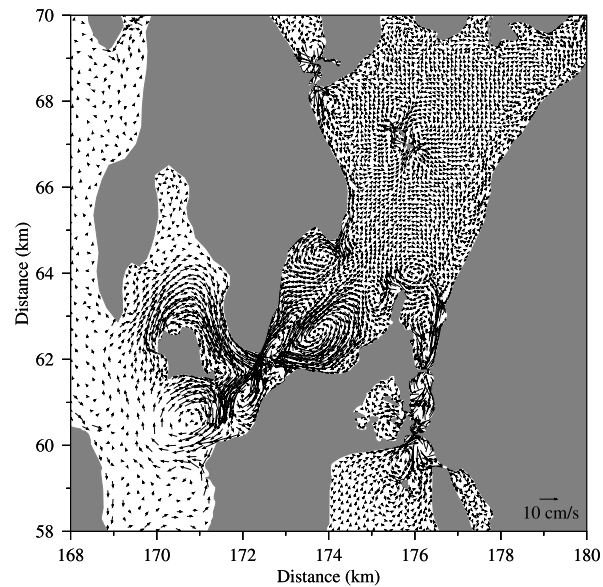

Figure 14. The distribution of the residual current for the model run with the five major tidal constituents (M_2, N_2, S_2, K_1, and O_1) forcing. The number of current points is reduced to produce a viewable picture.

MHB-NB channel. In the MHB-SR channel, a pair of residual eddies form on sides of SRB: cyclonic on the northern side and anticyclonic on the southern side. At SB, one cyclonic residual eddy is found on the northern side and a pair of cyclonic and anticyclonic residual eddies on the southern side, where the cross-channel length is much bigger than that on the northern side. Similar residual eddy features are also found in the passage linking the Kickamuit River to the MHB and around the Twin Spurs Island in the interior region of the MHB.

[32] Residual flow is weak in the interior away from islands and along the coast in the MHB, except on the western coast of the MHB where a remarkable southward residual current is detected along the coast. The occurrence of this coastal residual flow seems to be related to the existences of residual eddies around the coastal region of the Kickamuit River and the convex area in the downstream southwestern coast of the MHB.

4. Discussion

[33] Numerical experiments with FVCOM show that MHB-NB is characterized by strong tidal flushing and eddy shedding through deep channels and narrow necks. Model-predicted tidal flushing processes and eddy shedding in the MHB-NB channel are consistent with the theory, previous numerical experiment results and field measurements of tidal flushing in a narrow channel or estuary [*Stommel and Farmer*, 1952; *Wolanski et al.*, 1984; *Wells and Heijst*, 2003]. The theory and laboratory experiments suggest that when a current jet flows through a narrow channel, two vortices can be created on the lee side of the current outside the sharp channel as a result of the current separation. These two vortices may couple together to form a dipole when the direction of the current jet reverses and flow back into the channel [*Wells and Heijst*, 2003]. Two eddies, which are
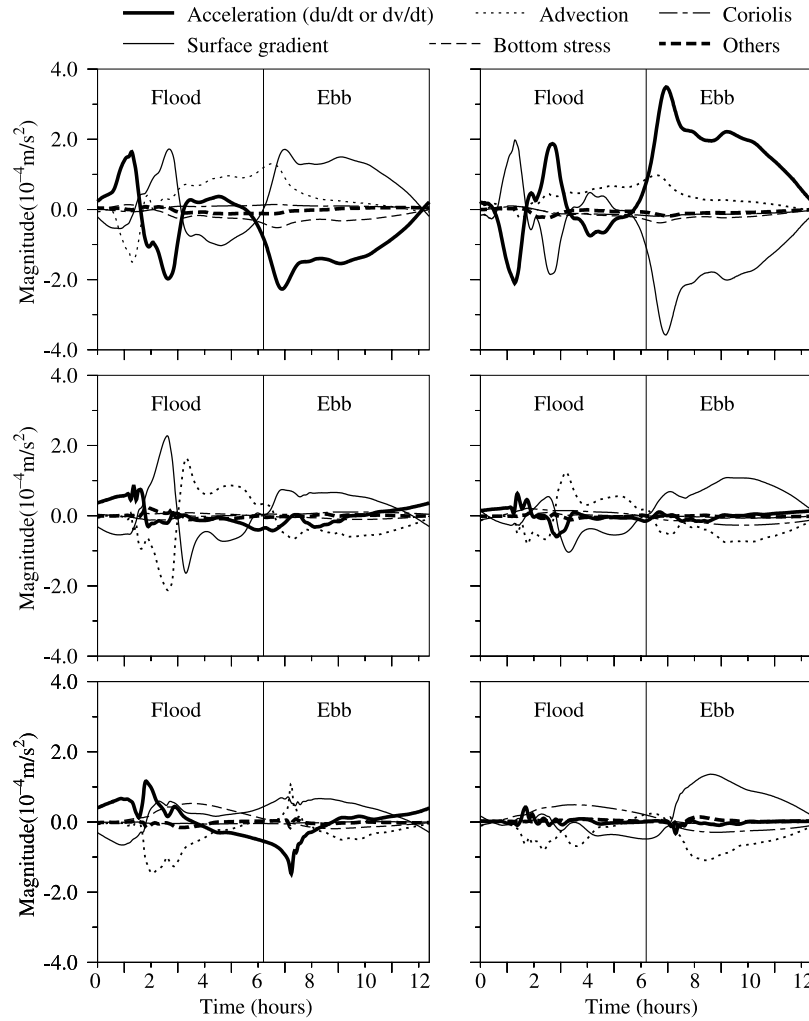
Figure 15. Time sequences of the terms in the along- (left) and cross- (right) isobath directions for vertically averaged momentum equations at selected points on transect T1 (shown in Figure 1).

predicted on the lateral side of the strong tidal current jet on the lee side of tidal flushing (during both flood and ebb periods) in our model, closely mimic the theoretical eddy shedding pattern. Unlike the classical laboratory experiment results summarized in *Wells and Heijst* [2003], the model does not show a coupling of these two eddies to form a dipole when the direction of tidal current reverses in our case. This is not surprising, because the lifetime of these two eddies are short, their intensities and scales are vastly different in the realistic geometric condition of the MHB-NB, and tidal mixing strongly varies in space and time over tidal cycles.

[34] The formation of the eddy due to the current separation at the headland was detected in many other coastal regions by direct current measurements. Example can be seen in the ADCP measurement around a headland in Vineyard Sound, Massachusetts made by *Geyer and Signell* [1990]. The observed current fields clearly show the formation of transient eddies on the lee side of the headland during flood and ebb due to the flow separation. The residual flow field is characterized by cyclonic and anticyclonic eddies on either side of the headland, with spatial scales of 5–8 km and maximum velocity of about 25 cm/s.

The structures of eddies around the convex coastline area or headland in the MHB-HB coast and islands predicted by FVCOM (see Figure 14) are very similar to those detected by Geyer and Signell, suggesting that by being able to accurately resolve the coastal boundaries, FVCOM is capable of resolving the formation of double eddy fields around the headland or other shelf region characterized by convex coastlines.

[35] To examine the physical process during the formation of the eddy, we made a momentum balance analysis on a cross-isobath transect cut through a region where a cyclonic eddy forms during the flood period (see T1 in Figure 1 for the location). In the inner shore area, one mesh point away from the coast, the local changes of vertically averaged, along- and cross-isobath velocities are controlled dominantly by the gradient of the surface elevation and nonlinear advection plus a first order contribution from the bottom stress (Figure 15: upper panels). In the flood tide, the gradient of the sea elevation modulates with a 3-hour oscillation, which directly causes the short-term oscillation of the velocity acceleration in both along- and cross-isobath directions. In the along-isobath direction, the advection shows a sharp change in the first 2 hours of the flood tide
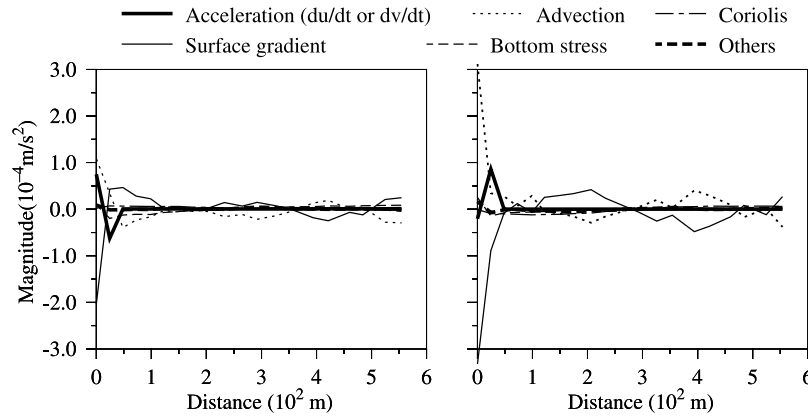
Figure 16. Distribution of the tidally averaged values of the terms in the along- (left) and cross- (right) isobath directions for vertically averaged momentum equations on transect T1 (shown in Figure 1).

and then gradually increases until the high water. This term drops rapidly in the early phase of the ebb period and becomes the second order term after the maximum ebb tide. The variation of the advection in the cross-isobath direction is very similar to that found in the along-isobath direction, except in the first 2 hours of the flood tide, where no a sharp change occurs in the cross-isobath advection. We find that the near-coastal current variability is primarily controlled by the variation of the sea level during the flood tide but during ebb tide, advection also plays an important role. This suggests that tidal motion near the coast is characterized by linear dynamics during the flood tide but by strong nonlinear process during the ebb tide.

[36] Near the center region of the eddy, during the flood period, the local change of the velocity is relatively small (Figure 15: mid-panels) A considerable acceleration of the cross-isobath current occurs in the first 2 hours of the flood tide as a result of a strong sea surface gradient. After that, the advective acceleration component grows quickly until it balances the gradient of the surface elevation after which no significant variation of the acceleration is found. In this area, the tidal motion is controlled by a weakly non-steady nonlinear process with the zero-order balance between advection and gradient of the surface level.

[37] At the outer edge of the eddy in the deep channel where the current separation occurs, the tidal motion is controlled by a strongly nonlinear process in which the advection is the dominant term driving the sharp change of flow acceleration during the early phase of the flood tide (Figure 15: lower panels). The fact that the sharp change of the acceleration is much larger in the cross-isobath direction than in the along-isobath direction, suggests that when the current separation occurs during the flood period, it can produce the large lateral advection to lead the energy transfer from current jet to the eddy.

[38] Averaging all terms in the momentum equations over a tidal cycle, we also examine the momentum balance on the transect T1 for the residual flow. It is clear that the residual eddy current is dominantly controlled by a balance between the gradient of the surface elevation and advection (Figure 16). The nonlinear advection seems to be a key process in the transfer of tidal energy into residual flow, and the cyclonic eddy residual current is built and maintained by adjustment of the sea level gradient to the advection. It

should be pointed out here that the residual current in the near-shore region with a width of 50 m does not reach a steady state. This means that the residual flow in that region changes during the tidal cycles. *Pawlak and MacCready* [2002] pointed out from their studies that the residual current could vary over tidal cycles if the eddies formed at the headland have a lifetime longer than a tidal cycle. That might not be a case for our finding in the near shore region across the intersection of MHB-NB, because the lifetime of the eddy formed in that area is shorter than half a tidal cycle. Our model does produce two eddies along the southwestern coast of the MHB (Figure 14). The non-steady residual flow field found in the near-shore region is probably related to the nonlinear interaction between these two eddies. The complex short-term variability found during the ebb tide at the western coast of the south-west end of MHB probably also is related to the interaction of these two eddies. A further investigation should be carried out to explore the physical mechanism driving the tide-induced, subtidal variation of the residual flow in the near shore region of the MHB.

[39] This configuration of FVCOM is the first physical model that is capable of resolving the eddy shedding process in the MHB-NB. It is important to inquire as to why previous finite-difference models used in this region failed in this effort. Since the dynamics described in FVCOM are the same as other finite-difference models, a simple answer for this question is geometric resolution. It is readily apparent that unstructured grids are able to better resolve the irregular coastlines of the MHB-NB. Because the current separation around headlands and islands is influenced by the coastal geometry, FVCOM, which utilizes unstructured grids, should have an advantage in resolving the formation of an eddy around a complex coastal region. However, it cannot explain why the finite-difference model fails to resolve the current separation in the MHB-NB channel since the eddy formation during the flood tide is manly controlled by the current separation in the deep channel. Previous finite-difference models were configured with horizontal resolution of about 200 m or larger. Such a horizontal resolution might not be able to resolve a big lateral shear of the horizontal current jet in the channel. To examine this issue, we have re-run FVCOM with coarse resolution meshes shown in Figure 2b, where the horizontal
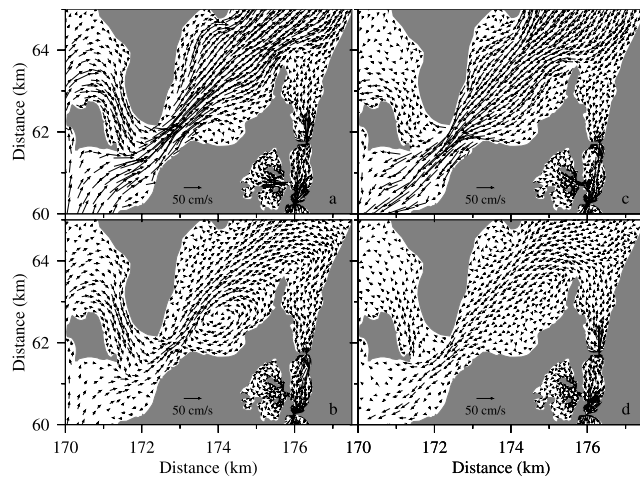
Figure 17. Distributions of the near-surface tidal currents at maximum flood, 3 hours after the maximum flood, maximum ebb, and 3 hours after the maximum ebb in the southern part of the MHB-NB-SR region for the model run with a coarse horizontal resolution of 200 m in both MHB-NB and MHB-SR channels.

resolution is reduced to 200 m in the MHB-NB channel region.

[40] The results clearly show that with the same geometric resolution of the coastline, the coarse model fails to resolve the cyclonic eddy on the western side of the current jet at the maximum flood (Figure 17a). At the same time, although it resolves the anticyclonic eddy on the eastern side, it is much weaker than one shown in the fine resolution case (Figure 17a). 3 hours after the maximum flood, the coarse resolution model does resolve two eddies on the either side of the current jet, but the intensity of these eddy are weaker and their spatial scales are also smaller (Figure 17b). In the ebb tide, no significant eddy fields are resolved in the lee side out of the channel like those shown in the finer resolution cases, even though very weak eddy fields can be still recognized on the northern side at maximum ebb and later and on the southern side 3 hours after the maximum ebb (Figures 17c and 17d).

[41] This comparison experiment suggests that in addition to the coastal geometric fitting, horizontal resolution also is a key factor that controls the current separation. Since most of the coastal ocean models use the Smagorinsky turbulent closure schemes to parameterize the horizontal diffusion, the horizontal diffusion in the model decreases with mesh sizes. The reduced intensity of eddies in the coarse resolution case is also related to the increased horizontal diffusion due to the decrease of the horizontal resolution.

[42] Since the eddy shedding is sensitive to the horizontal resolution used in the model, a sensitivity study should be always conducted to find a minimum horizontal resolution at which a numerical solution converges. Previously these experiments have been impractical due to limited compute power but such a study will become feasible in the near future. Since the minimum requirement for horizontal resolution depends on the scale of the motion, which varies in space, the unstructured grid model seems more flexible for such an application. For examples, in the MHB-NB, the fine resolution is required only in the narrow channels, around islands, and rivers. Configuring the MHB-NB model with unstructured grids not only ensure the minimum requirement for horizontal resolution, but also significantly increases the computational efficiency.

5. Summary

[43] The tidal motion in the Mt. Hope Bay (MHB) and Narragansett Bay (NB) is simulated using the unstructured grid, finite-volume coastal ocean model (FVCOM). With an accurate geometric representation of irregular coastlines and islands and sufficient high horizontal resolution in narrow channels or passages, FVCOM provides an accurate simulation of the tidal wave in the bays and tidal flushing process through the MHB-NB and MHB-SR channels. Eddy shedding occurs on the lee side of tidal flushing due to current separation during both flood and ebb tides These eddies grow in both size and intensity in 3 hours after the maximum flood or maximum ebb. Because of the eddy formation, the vertical profile of the tidal current varies significantly during tidal cycles. Strong vertical shear of the current occurs in the late phase of the flood period.

[44] The tidal flushing in the MHB-NB channel has a direct impact on the current in the MHB-SR channel. The interaction between these channels causes a 90° phase leading in the water transport in the MHB-SR channel than in the MHB-NB channel, even though the water transport ratio of these two channels is only about 10−20%.

[45] The residual flow field in the MHB and NB is featured by multiple eddies around headlines, convex and concave coastline regions, around islands, channels and near river mouths. The formation of these eddies are mainly due to the current separation either at the tip of the coastlines or asymmetric tidal flushing in narrow channels or passages.

[46] Process-oriented modeling experiments show that horizontal resolution plays a critical role in resolving the asymmetric tidal flushing process through narrow passages. With a horizontal resolution of 50 m, FVCOM reproduces an eddy field that is similar to the velocity profile suggested by the ship-mounted ADCP measurements reported in *Kincaid* [2006].

[47] Momentum balances suggest that the dynamics controlling the current in eddies varies significantly over tidal cycles. Residual eddies, formed as a result of tidal flushing in the deep channel of the MHB-NB, are controlled by a balance between the nonlinear advection and gradient of the sea surface elevation. Due to strong nonlinearity and interaction between eddies; the residual eddy flow in the nearshore region doesn't reach equilibrium.

[48] The FVCOM results are consistent with the theory of tidal flushing and are also in good agreement with the limited current measurement data available in the MHB. This modeling experiment provides a guide for further direct field measurements. The model-predicted multiple residual eddy field suggests that the water exchange between the MHB and NB is much more complex than previously understood.

References

Bergondo, D., D. R. Kester, H. E. Stoffel, and W. L. Woods (2005), Time series observations during the low sub-surface oxygen events in Narragansett Bay during summer 2001, *Mar. Chem.*

Chen, C., H. Liu, and R. Beardsley (2003), An unstructured grid, finite-volume, three-dimensional, primitive equations ocean model: Application to coastal ocean and estuaries, *J. Atmos. Ocean Technol.*, 20(1), 159–186.

Chen, C., G. Cowles, and R. C. Beardsley (2004), An unstructured grid, finite-volume coastal ocean model: FVCOM user manual, *SMAST/UMASSD Tech. Rep.*, 04-0601, 183 pp.

Deacutis, C. F., D. W. Murray, W. L. Prell, E. Saarman, and L. Korhun (2006), Hypoxia in the upper half of Narragansett Bay, RI during August 2001 and 2002, *Northeast Naturalist*, in press.

Foreman, M. G. G. (1977), Manual for tidal heights analysis and prediction, *Pac. Mar. Sci. Rep. 77-10*, 58 pp., Inst. of Ocean Sci., Patricia Bay, Sidney, B. C.

Galperin, B., L. H. Kantha, S. Hassid, and A. Rosati (1988), A quasi-equilibrium turbulent energy model for geophysical flows, *J. Atmos. Sci.*, 45, 55–62.

Geyer, W. R., and R. Signell (1990), Measurements of tidal flow around a headland with a shipboard account Doppler current profiler, *J. Geophys. Res.*, 95, 3189–3197.

Gordon, R. B., and M. L. Spaulding (1987), Numerical simulations of the tidal- and wind-driven circulation in Narragansett Bay, *Estuarine Coastal Shelf Sci.*, 24, 611–636.

Gray, S. M. (1884), Proposed plan for a sewerage system and for the disposal of the sewage of the City of Providence, 25.

Haight, F. J. (1938), Currents in Narragansett Bay, Buzzards Bay, and Nantucket and Vineyard Sounds, U.S. Coast and Geodetic Survey, *Spec. Publ.*, 208, 101 pp.

Hicks, S. D. (1959), The physical oceanography of Narragansett Bay, *Limnol. Oceanogr.*, 11, 316–327.

Kincaid, C. (2006), The exchange of water through multiple entrances to the Mt. Hope Bay estuary, *Northeast Naturalist*, in press.

Mellor, G. L., and T. Yamada (1982), Development of a turbulence closure model for geophysical fluid problem, *Rev. Geophys.*, 20, 851–875.

Nixon, S. W., S. Granger, B. A. Buckley, M. Lamont, and B. Rowell (2004), A one hundred and seventeen year coastal water temperature record from Woods Hole, Massachusetts, *Estuaries*, 27, 397–404.

Pawlak, R. D., and P. MacCready (2002), Oscillatory flow across an irregular boundary, *J. Geophys. Res.*, 107(C5), 3036, doi:10.1029/2000JC000596.

Smagorinsky, J. (1963), General circulation experiments with the primitive equations, I. The basic experiment, *Mon. Weather Rev.*, 91, 99–164.

Spaulding, M. L., D. L. Mendelsohn, and J. C. Swanson (1999), WQMAP: An integrated three-dimensional hydrodynamic and water quality model system for estuarine and coastal applications, *MTS J.*, 33(3), 38–54.

Stommel, H., and H. G. Farmer (1952), On the nature of estuarine circulation, *WHOI Tech. Rep.*, 52-88, 131.

Swanson, J. C., and K. Jayko (1987), Preliminary results from a simplified numerical model of Narragansett Bay, Rhode Island (from ASA), *Oceans' 87 Proc.*, 3, 843–846.

Weisberg, R. H. (1976), The nontidal flow in the Providence River of Narragansett Bay: A stochastic approach to estuarine circulation, *J. Phys. Oceanogr.*, 6, 721–734.

Weisberg, R. H., and W. Sturges (1976), Velocity observations in the West Passage of Narragansett Bay: A partially mixed estuary, *J. Phys. Oceanogr.*, 6, 345–354.

Wells, M. G., and G. J. F. V. Heijst (2003), A model of tidal flushing of an estuary by dipole formation, *Dyn. Atmos. Oceans*, 37, 223–244.

Wolanski, E., J. Imberger, and M. Heron (1984), Island wakes in shallow coastal water, *J. Geophys. Res.*, 89, 10,553–10,569.

_____

C. Chen, G. Cowles, and L. Zhao, School for Marine Science and Technology, University of Massachusetts at Dartmouth, 706 South Rodney French Blvd., New Bedford, MA 02744, USA. (lzhao@umassd.edu)